ELSEVIER

Materials Science and Engineering A268 (1999) 184–192

MATERIALS SCIENCE & ENGINEERING A

Cracking in Cr–Cr_2Nb eutectic alloys due to thermal stresses

Sanboh Lee [a,*], P.K. Liaw [b], C.T. Liu [c], Y.T. Chou [a,1]

[a] *Department of Materials Sciences, National Tsing Hua University, Hsinchu, Taiwan*
[b] *Department of Materials Science and Engineering, University of Tennessee, Knoxville, TN 37996-2200, USA*
[c] *Metals and Ceramics Division, Oak Ridge National Laboratory, Oak Ridge, TN 37831-6115, USA*

Received 19 October 1998; received in revised form 26 January 1999

Abstract

The microstructures of the Cr–Cr_2Nb two-phase alloy as affected by thermal stresses have been investigated for three different systems: (1) Cr-rich particles surrounded by the eutectic network; (2) Cr_2Nb particles embedded in the Cr-rich matrix; and (3) Cr-rich particles inside the Cr_2Nb matrix. Micrographs of the as-cast and annealed specimens show that microcracks are primarily located at the interface between the particle and the matrix. These observations are related to the presence of thermal stress field of elastic inclusions with its maximum tensile and shear stresses located at the interface boundary. The theoretical analyses presented support the formation of crack embryos at the interface as the local tensile stress exceeds the critical value for crack nucleation. © 1999 Elsevier Science S.A. All rights reserved.

Keywords: Thermal stress; Eutectic network; Cr-rich matrix; Cr_2NB matrix; Microcracks

1. Introduction

Dual-phase alloys based on Cr–Cr_2Nb and Cr–Cr_2X (where X is a refractory element, such as Zr, Hf, etc.) are currently being studied for high-temperature structural applications. These alloys are of technological interest because they possess excellent high-temperature strength, good high temperature oxidation and possible corrosion resistance [1], and relatively low material density [2]. The Laves phase, Cr_2Nb, with the C15 complex cubic crystal structure has excellent high temperature strength and creep resistance, but it is very hard (8 GPa) and brittle at room temperature [3]. The phase diagram of the Cr–Nb system given in Fig. 1. Takeyama and Liu, and Thoma and Perepezko [3,4] show the formation of a eutectic structure consisting of a Cr solid solution phase and a Cr_2Nb Laves phase, with the eutectic reaction occurring around 1668°C at the composition of 18.5 at.% Nb. This phase relationship suggests the possibility of using the eutectic alloy for better toughness [3,5–8]. At present, a considerable effort is devoted to the study of microstructural control and development of two-phase Cr–Cr_2Nb alloys for structural applications.

In the study of two-phase Cr–Cr_2Nb alloys, both micro and macro cracks were observed in alloy ingots. Additional cracking was also observed when the alloys were cooled down from heat treatment at temperatures below the eutectic temperature. Thermal stresses were

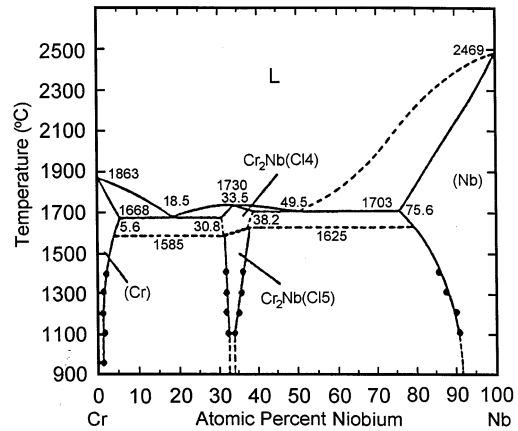

Fig. 1. The Cr–Nb phase diagram.

* Corresponding author. Tel.: +886-3-5719677; fax: +886-3-5722366.

E-mail address: sblee@mse.ntu.edu.tw (S. Lee)

[1] On leave from the Department of Materials Science and Engineering, Lehigh University, Bethlehem, PA 18015, USA.

0921-5093/99/$ - see front matter © 1999 Elsevier Science S.A. All rights reserved.
PII: S0921-5093(99)00068-4

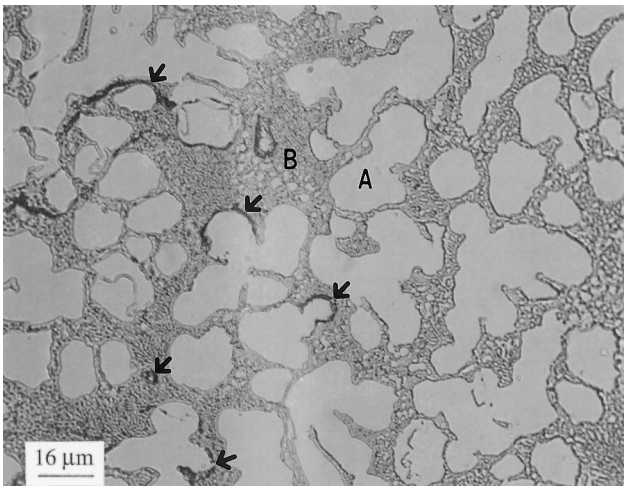

Fig. 2. Optical micrograph of an as-cast CN-4 binary alloy. (A) Cr-rich solid solution; (B) Cr–Cr_2Nb eutectic phase, and arrow mark, microcrack.

generated either by cooling from the cast state or heat treatment at lower temperatures. Generally, the heat treatment did not cause any change in microstructure, except for the precipitation of fine Cr_2Nb particles in primary Cr patches and the coarsening of Cr-rich particles in the eutectic matrix. The presence of thermal stresses between the Cr-rich and Cr_2Nb phases has been suggested to be a cause of such cracking; however, there is no theoretical analysis to provide a possible mechanism for cracking in Cr–Cr_2Nb alloys during casting and subsequent heat treating. It is the objective of this study to demonstrate that the maximum stresses generated from thermal mismatch are sufficiently high to cracking the Cr–Cr_2Nb alloy. In the present investigation, a metallographic examination on cracking behavior, in conjunction with a theoretical calculation of thermal stresses, is performed to identify the cause of crack nucleation and propagation in the dual-phase alloy.

2. Microstructural features and cracking

The Cr–Nb alloy, used in this study, contains 12 at.% Nb and is designated as the CN-4 alloy. The experimental procedure is similar to that reported by Takeyama and Liu [3]. The ingot was prepared by arc-melting and drop-casting into a chilled copper mold in an argon atmosphere. It was subsequently heat treated to obtain various microstructures. Fig. 2 shows an optical microstructure of the binary alloy of a hypoeutectic composition: Nb < 33.3 at.%, where the patches of Cr-rich solid solution (region A) are surrounded by the interconnected Cr–Cr_2Nb eutectic structure indicated by region B. Previous results using transmission electron microscopic and electron microprobe analyses indicated that the Cr-rich patches contain 5.5 at.% Nb [6], which is almost equal to the maximum Nb solubility at the eutectic temperature of 1668°C. This observation suggests that the cooling rate associated with the drop casting of alloy ingots in a copper mold is high enough to suppress the precipitation of Cr_2Nb from the Cr-rich patches. According to the equilibrium phase diagram shown in Fig. 1, the Cr-rich phase in the cast alloy is in a highly supersaturated condition which is embrittled by the excess of Nb, a solute with an atomic size (14.7 nm) significantly larger than that of Cr (12.8 nm). As shown in Fig. 2, microcracks, indicated by arrows, are generally nucleated at the interfaces between the Cr-rich patch and the eutectic network. A microcrack is also formed around the coarse Cr-rich particles embedded in the Cr_2Nb phase within the eutectic structure. Fig. 3 shows a microcrack indicated by the arrow in as-cast CN-4 alloy which generally propagated along the interfaces of the eutectic matrix and Cr-rich patches and in the eutectic matrix. Similar cracking behavior was observed in the Cr–Cr_2Nb alloys containing 6 at.% Nb [6]. In general, the frequency of cracking increases with increasing Nb concentration or Cr_2Nb volume fraction. This is because the increase of Nb will increase the amount of the brittle Cr_2Nb phase and reduce the soft Cr-rich solid solution, which is available to absorb thermal stresses generated in the material [3,15].

The supersaturated Cr-rich solid-solution patches would precipitate out the fine Cr_2Nb particles after annealing below the eutectic temperature. Fig. 4 is a scanning electron micrograph showing the fine precipitates formed in a CN-4 specimen annealed for 100 h at 1100°C plus 5 days at 900°C [3]. Note that the Cr_2Nb particles are so fine that they can not be identified by optical metallography (Fig. 5). Microcracks (or holes),

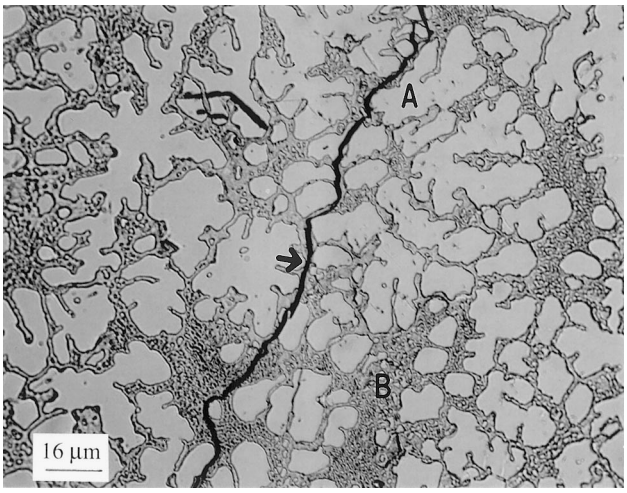

Fig. 3. A microcrack (indicated by the arrow) propagates along the interface between Cr-rich solid solution and eutectic phase and inside the eutectic matrix in an as-cast CN-4 alloy.

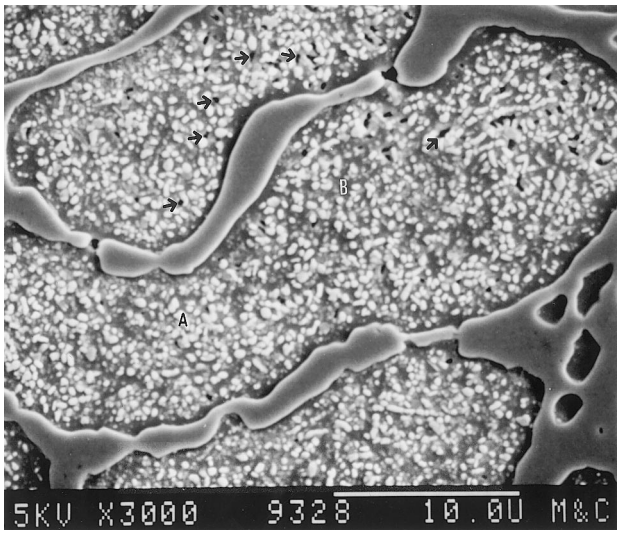

Fig. 4. A scanning electron micrograph showing fine Cr_2Nb particles in a CN-4 alloy annealed at 1100°C for 100 h and 900°C for 5 days [3]. Black dots are microcracks indicated by the arrows.

indicated by arrows in Fig. 5, were formed in the eutectic network in this annealed specimen which might also be nucleated at the interfaces of Cr-rich particles surrounded by the Cr_2Nb matrix (Fig. 4). Fig. 6 shows an optical micrograph of a CN-4 specimen after annealing for 1 h at 1350°C and 5 days at 900°C in vacuum (region A and region B are Cr-rich solid solution and Cr_2Nb network, respectively). A macrocrack has propagated mainly along the interfaces of the Cr-rich patches and the Cr_2Nb phase, and also in the Cr_2Nb network.

The above metallographic examination indicates that the microcracks are primarily nucleated at: (1) the interfaces between the Cr-rich patches and the eutectic network; (2) between the fine Cr_2Nb particles and Cr-rich patches; and (3) between the Cr-rich particles and

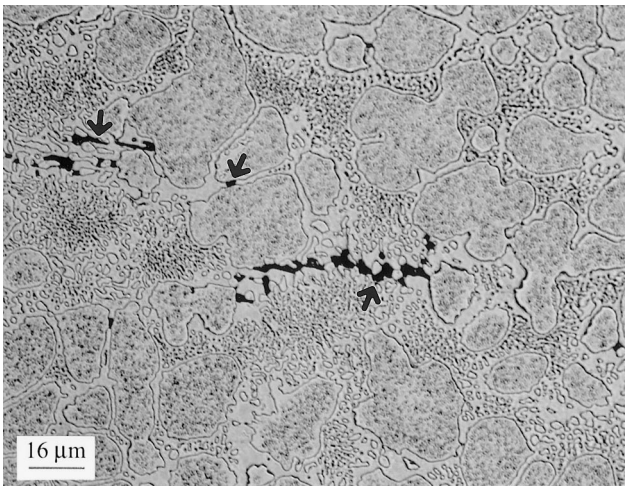

Fig. 5. An optical micrograph showing microcracks indicated by arrows in a CN-4 alloy annealed at 1100°C for 100 h and 900°C for 5 days.

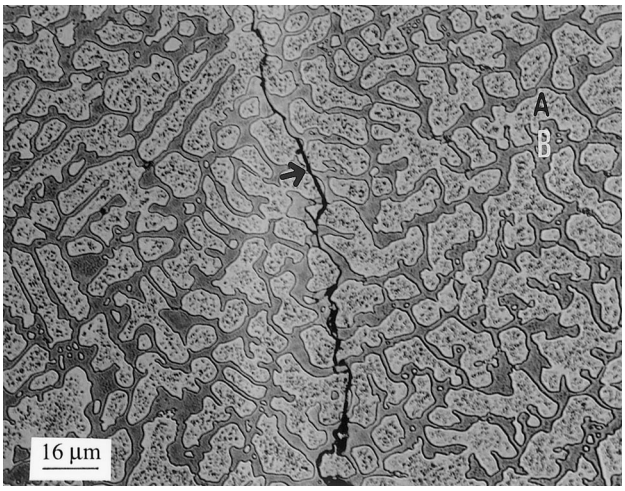

Fig. 6. A macrocrack indicated by the arrow propagates along interface and in the Cr_2Nb network in a CN-4 alloy annealed at 1350°C for 1 h and 900°C for 5 days. Region A is the Cr-rich particle and region B the Cr_2Nb matrix.

Cr_2Nb matrix in the eutectic network. The propagation of these cracks results in the final fracture of alloy specimens.

3. Results of thermal stress analysis

The occurrence of micro- and macro-cracks in the $Cr-Cr_2Nb$ two-phase alloy can be explained by the presence of thermal stress generated after the heat treatment. The two-phase microstructure can be considered as an inhomogeneous elastic system, in which a spheroidal inclusion is embedded in an infinite matrix. The inclusion has a thermal expansion coefficient α^*, shear modulus μ^* and Poisson's ratio ν^*, which are different from those of the matrix denoted by α, μ and ν. Because of the differences in thermal and elastic response, a thermal stress field would be set up upon a temperature change. Such a problem has been solved by Edwards [9]. However, his results are expressed in the curvilinear coordinates which are inconvenient for illustration. On the other hand, the same problem can be more effectively solved in the Cartesian coordinate system by the method of Eshelby [10–12]. We propose a new relation between prolate spheroid coordinates and Cartesian coordinates in which a function can be easily transformed from the prolate spheroid coordinates to the oblate spheroid coordinates. The new results derived based on the prolate spheroid coordinates are given in the Appendix A and will be used in the present analysis of thermal cracking.

From the experimental observations, three different inclusion systems as shown in Fig. 7 (i–iii), need to be investigated: (i) a Cr-rich spheroidal particle in an eutectic structure; (ii) a Cr_2Nb particle in a Cr-rich

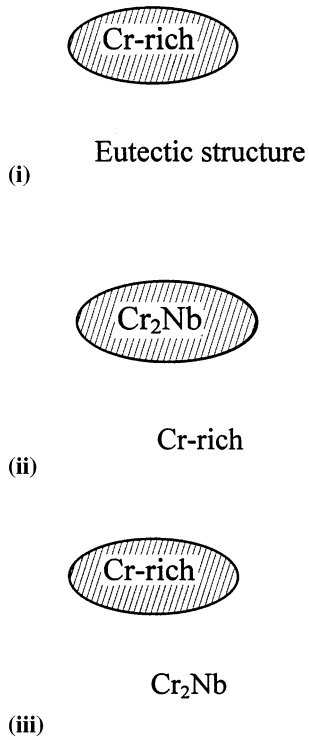

Fig. 7. Three inclusion systems: (i) a Cr-rich particle in a eutectic structure; (ii) a Cr_2Nb particle in a Cr-rich matrix; and (iii) a Cr-rich particle in a Cr_2Nb matrix. The inclusions lie in shaded areas.

matrix; and (iii) a Cr-rich particle in a Cr_2Nb matrix. The analyses and results are given in the following.

3.1. Cr-rich inclusion in the eutectic structure

We first consider the case of a Cr-rich particle as a spheroidal inclusion embedded in the eutectic structure (see Fig. 7(i)). The physical and mechanical parameters of the Cr–Cr_2Nb alloy are listed in Table 1 [13,14]. From the table the thermal expansion coefficients and elastic moduli of Cr_2Nb and Cr are $8.7 \sim 11.8$ μm m^{-1} K^{-1}, 220 GPa and 6.2 μm m^{-1} K^{-1}, 248 GPa, respectively. We choose the thermal expansion coefficient of Cr_2Nb to be 10 μm m^{-1} K^{-1}. The thermal expansion coefficient and elastic modulus of the eutectic structure are calculated as 8.15 μm m^{-1} K^{-1} and 234 GPa based on the rule of mixtures. A temperature drop from 1668 to 25°C leads to the thermal mismatch $(\alpha^* - \alpha)T = 3.2$ mm m^{-1} [15]. Assuming that both the inclusion and matrix have the same Poisson's ratio $\nu = 0.3$, we have $m = \mu^*/\mu = 1.06$.

Table 1
Physical and mechanical parameters of *Cr–Cr₂Nb* alloy

	Cr_2Nb	*Cr*
Thermal expansion coefficient (μm $m^{-1}K^{-1}$)	8.7	6.2
	~ 11.8	
Elastic modulus at 20°C (GPa)	221	248
Tensile strength at 20°C (MPa)	220	83
Melting point (°C)	1730	1857
Eutectic point (°C)	1668	–
Lattice constant (Å)	6.78	2.88

As shown in the Appendix A, the stresses inside the spheroidal inclusion are uniform and the maximum stresses are located at the interface. The principal stresses at the interface are plotted in Fig. 8(a) with $m = 1.06$. The superscripts, I and E, refer to the curves of stress components inside the inclusion and at the interface when approaching from the matrix, respectively, and the semimajor and semiminor axes (at the interface) are $x_1 = a$ and $x_3 = c$. It should be noted that the force is continuous at the interface, that is, $\sigma_{11}^I = \sigma_{11}^E = (x_1 = a)$ and $\sigma_{33}^I = \sigma_{33}^E = (x_3 = c)$. The stresses ($\sigma_{11}^I$ and σ_{33}^I) inside the inclusion are uniform and compressive for all aspect ratios, $k(= c/a)$. The value of σ_{11}^I increases with increasing k, and the trend for σ_{33}^I is the opposite. The curve of $\sigma_{33}^E(x_1 = a)$ increases to a maximum, and then decreases with increasing k, but the values of $\sigma_{33}^E(x_3 = c)$ and $\sigma_{33}^E(x_1 = a)$ increase monotonically with k. The magnitude of the stress in the matrix decreases with increasing distance away from the interface. It is reasonable to assume that if the tensile stress is greater than the critical tensile stress for creating a crack nucleus, a crack embryo could be formed. Because $\mu(\alpha^* - \alpha)T$ is equal to 749 MPa and the maximum tensile stress is $\sigma_{33}^E(x_1 = a)$ if $k \leq 1$ and $\sigma_{22}^E(x_1 = a)$ if $k \geq 1$, the maximum tensile stress is greater than 288 MPa ($k = 1$). This value is greater than the tensile strengths of the Cr-rich (83 MPa) and Cr_2Nb (220 MPa) phases. The measured tensile strength 220 MPa of Cr_2Nb is assumed to be the fracture stress in view of the fact that the alloy is very brittle with little elongation. When the maximum tensile stress at the interface (≥ 288 MPa) is greater than the macro fracture stress, it would be natural for a crack embryo to be nucleated at this site (interface) than any other sites. As a result, cracks would be formed at the interface between the Cr-rich particle and eutectic structure, as indicated by arrows in Figs. 2 and 5.

According to the Tresca criterion [12], yielding occurs when the shear stress reaches a critical value in the uniaxial tensile test. From the appendix, the shear stress components at interface are zero. Based on the Mohr circle, the shear stresses, $\sigma_{13}^I = [\sigma_{11}^I - \sigma_{33}^I]/2$, $\sigma_{12}^E(x_1 = a) = [\sigma_{11}^I - \sigma_{22}^E(x_1 = a)]/2$, $\sigma_{13}^E(x_1 = a) = [\sigma_{11}^I - \sigma_{33}^E(x_1 = a)]/2$, $\sigma_{23}^E(x_1 = a) = [\sigma_{22}^E(x_1 = a) - \sigma_{33}^E(x_1 = a)]/2$, and $\sigma_{13}^E(x_3 = c) = [\sigma_{11}^E(x_3 = c) - \sigma_{33}^I]/2$, are plotted in Fig. 8(b). The values of σ_{13}^I and $\sigma_{13}^E(x_3 = c)$ increase monotonically with k. The curves of $\sigma_{13}^E(x_3 = a)$ and $\sigma_{23}^E(x_3 = a)$ decrease to a minimum, and then increase with increasing k. The value of $\sigma_{13}^E(x_1 = a)$ increases

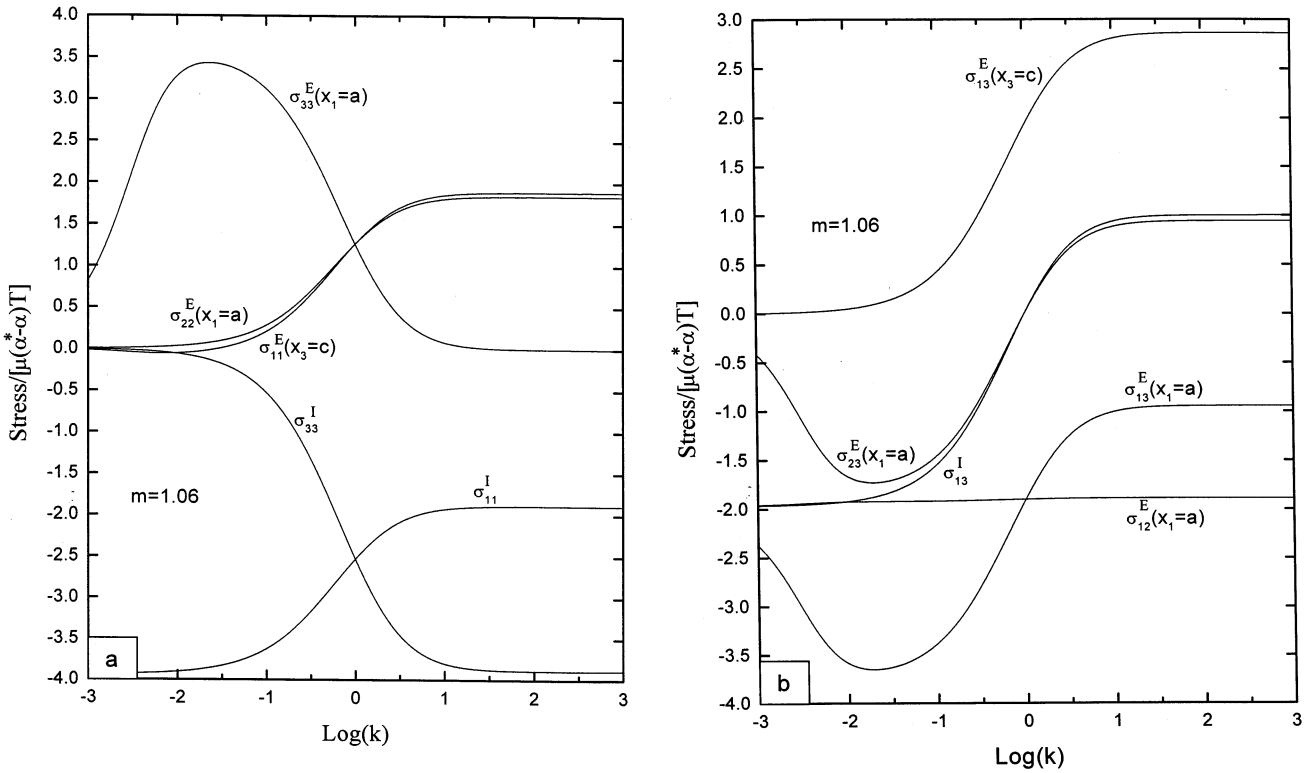

Fig. 8. (a) Principal stresses and (b) shear stresses at the interface between the Cr-rich particle and eutectic structure in a Cr–Cr_2Nb alloy.

slightly with increasing k. It is seen from Fig. 8(b) that for a given k, the maximum shear stress is $\sigma_{13}^{E}(x_1 = a)$ for $k \leq 1$ and $\sigma_{13}^{E}(x_3 = c)$ for $k \geq 1$. That is, the maximum shear stress is in the range of 2620 MPa ($k = 0.019$) and 1420 MPa ($k = 1$). Such large shear stresses would be able to create dislocations and form crack embryos because the specimens fractured before reaching the yield point. Although the direct observation of such a dynamic process is a difficult task and has to be performed in situ in a transmission electron microscope, it is a well-accepted concept that when the maximum shear stress is greater than the critical stress to generate dislocations, a dislocation pileup would be formed. If the stress concentration at the head of the pileup exceeds the cohesive stress of atoms, a microcrack would be nucleated in this region. This model seems to be valid in this case (Figs. 2 and 5).

3.2. Cr_2Nb inclusion in the Cr-rich matrix

We next consider the Cr_2Nb phase as the spheroidal inclusion embedded in the Cr-rich matrix as schematically shown in Fig. 7(ii). As stated in Section 3.1, the thermal expansion coefficients and elastic moduli of Cr_2Nb and Cr are estimated as 10 μm m^{-1} K^{-1}, 221 GPa and 6.2 μm m^{-1} K^{-1}, 248 GPa, respectively. A temperature drop from 1100 to 25°C gives $(\alpha^* - \alpha)T = -4.085$ mm m^{-1} [16]. At $\nu = \nu^* = 0.3$, we have $m = \mu^*/\mu = 0.89$ with the shear modulus (μ or μ^*) equal to the Young's modulus divided by $2(1 + \nu)$. The variation of the principal stresses on the interface with $m = 0.89$ is very similar to that in the previous case. The stresses in the inclusion are always tensile regardless of the aspect ratio, k. The curve of σ_{11}^{I} increases with increasing k, but the trend of σ_{33}^{I} is reversed. The stress components, $\sigma_{22}^{E}(x_1 = a)$, $\sigma_{33}^{E}(x_1 = a)$ and $\sigma_{11}^{E}(x_3 = c)$, are compressive for all values of k. The curves of $\sigma_{22}^{E}(x_1 = a)$ and $\sigma_{11}^{E}(x_3 = c)$ increase to a maximum, and then decrease with increasing k, but the variation of $\sigma_{33}^{E}(x_1 = a)$ is opposite. The magnitude of the stress in the matrix decreases with increasing distance away from the interface (see Appendix A). The value of $\mu(\alpha^* - \alpha)T$ is equal to 389 MPa. The maximum tensile stress is σ_{11}^{I} if $k \leq 1$ or σ_{33}^{I} if $k \geq 1$. As a result, the maximum tensile stress is greater than 490 MPa ($k = 1$). Again, assume that the fracture stress is equal to the tensile strength ($= 220$ MPa) of the Cr_2Nb listed in Table 1. Since the value of maximum tensile stress is greater than the assumed macro fracture stress, a crack embryo would prefer to be formed inside the Cr_2Nb inclusion or along the interface, but not in the Cr-rich matrix. This is because that there is no tensile stress inside the ductile Cr-rich matrix during the high temperature annealing. The explanation is supported by the observation of black dots shown in Fig. 4 in which the crack embryos were formed along the interface of the Cr_2Nb particle and the Cr-rich matrix as indicated by arrows.

Using the method of the Mohr circle, the shear stresses, σ_{13}^{I}, $\sigma_{12}^{E}(x_1=a)$, $\sigma_{13}^{E}(x_1=a)$, $\sigma_{23}^{E}(x_1=a)$, and $\sigma_{13}^{E}(x_3=c)$, were determined, and their variations are similar to those in Fig. 8(b). Both $\sigma_{13}^{E}(x_1=a)$ and $\sigma_{23}^{E}(x_1=a)$ decrease to a minimum, and then increase with increasing k, while the components, σ_{13}^{I} and $\sigma_{13}^{E}(x_3=c)$ increase monotonically with k. On the other hand, the variation of $\sigma_{12}^{E}(x_1=a)$ is almost independent of k. For a given k, the maximum shear stress is $\sigma_{13}^{E}(x_1=a)$ if $k \leq 1$ and $\sigma_{13}^{E}(x_3=c)$ if $k \geq 1$. This is equivalent to the maximum shear stress having a range of 1.35 GPa ($k=0.022$) and 700 MPa ($k=1$). Using the argument given in the preceding subsection, a dislocation pileup would be formed and subsequently induce the formation of crack nuclei when the maximum shear stress is greater than the critical stress for generating dislocations. The interface would be the preferred site to produce microcracks because of the presence of the maximum shear and normal stresses.

3.3. Cr-rich inclusion in the Cr_2Nb matrix

In the third case, the Cr-rich particle is considered as a spheroidal inclusion embedded in the Cr_2Nb phase, as shown in Fig. 7(iii). The physical parameters are the same as those in the previous subsections. A temperature drop from 1350 to 25°C gives $(\alpha^*-\alpha)T=-5.03$ mm m^{-1} [15]. Using the same Poisson's ratio, $\nu=0.3$, we have $m=\mu^*/\mu=1.12$. The variations of principal stresses at the interface are similar to those for $m=1.06$. The stresses inside the inclusion are uniform and compressive for all k. The maximum tensile stress is $\sigma_{33}^{E}(x_1=a)$ if $k \leq 1$ and $\sigma_{22}^{E}(x_1=a)$ if $k \geq 1$. Because the value of $\mu(\alpha^*-\alpha)T$ is equal to 429 MPa, the maximum tensile stress is greater than 553 MPa ($k=1$). Again, assume that the fracture stress is equal to the tensile strength ($=220$ MPa) of the Cr_2Nb. As the maximum tensile stress is greater than the critical tensile stress for fracture, a crack embryo is nucleated. This prediction is supported by the micrograph shown in Fig. 6 in which a crack is passing through the interface between the Cr-rich particle and Cr_2Nb matrix.

From the Mohr circle, the shear stresses, σ_{13}^{I}, $\sigma_{12}^{E}(x_1=a)$, $\sigma_{13}^{E}(x_1=a)$, $\sigma_{23}^{E}(x_1=a)$, and $\sigma_{13}^{E}(x_3=c)$, are calculated at $m=1.12$ and their variations are similar to those in the previous cases. For a given k, the maximum shear stress is $\sigma_{13}^{E}(x_1=a)$ for $k \leq 1$ and $\sigma_{13}^{E}(x_3=c)$ for $k \geq 1$. That is, the maximum shear stress is in the range of 831 MPa ($k=1$) and 1605 MPa ($k=0.018$). As mentioned in the preceding subsections, we may assume that the stress concentration at the head of a dislocation pileup would create a crack embryo, and the preferable place for the pileup is at the interface where the shear stress is maximum.

4. Discussion

The numerical calculations presented above show that the principal stresses and maximum shear stresses at the interface have similar characteristics for all three cases with difference in magnitude and sign. From the Tresca criterion, plastic deformation will occur when the shear stress is greater than the critical resolved shear stress. This also implies the generation of dislocations. The point where the maximum shear stress is located is most probably the source of dislocations. A dislocation pileup would be formed here against the interface and induce a crack embryo [17,18]. Stroh [19] quantitatively analyzed that if the stress concentration at the head of the dislocation pileup is not relaxed by plastic deformation, then the enhanced tensile stress at the head of the piled-up group would exceed the cohesive strength and lead to nucleation of microcracks. The dislocation structure in C15 $Cr-Cr_2Nb$ alloy has recently been studied by Kumar and Liu [15]. Evidently, in the absence of strong pinning centers, the dislocation pileups were not observed in the specimens.

We have assumed that in our proposed model, a single inclusion is placed in an infinite matrix, even though it deviates from the real system we observed. The deviation is caused by two geometrical effects. The first is the surface effect, which however, would relax the induced thermal stress and reduce embrittlement. Furthermore, Seo and Mura [20] have pointed out that when the free surface is situated from the inclusion at a distance three times of the particle size, its effect would be negligible. The second effect is concerned with the spacing between the neighboring inclusions. A finite separation would yield a higher thermal stress. Thus the calculated results presented above should be considered as the lower limits for the real system.

The thermal stress model presented above is valid only before the crack is formed. After the crack nucleus appears, the problem should be treated using the linear elastic fracture mechanics. According to fracture mechanics, a crack would propagate when the stress intensity factor at the crack tip is greater than the stress intensity factor for crack growth [21–23]. The growth direction is always toward the region of the tensile stress. Therefore, the crack would grow along the interface of the Cr-rich patch and eutectic structure and within the eutectic structure as shown in Fig. 3. Or the crack would grow along the interface between the Cr-rich particle and Cr_2Nb matrix and within the Cr_2Nb matrix as exhibited in Fig. 6.

Although the thermal expansion coefficient is a function of temperature, we have chosen the thermal expansion coefficient of Cr_2Nb as 10 μm m^{-1} K^{-1} instead of the lower bound of 8.7 μm m^{-1} K^{-1} and upper bound of 11.8 μm m^{-1} K^{-1} as listed in Table 1. If we use both of the limits to calculate the thermal stresses for

the above three cases, the trend will be the same except for slight changes of the magnitude.

It has been noted that the frequency of cracking increases with increasing Nb concentration in hypo-eutectic alloys [3]. The cause is obvious. From the phase diagram in Fig. 1, the amount of Cr-rich phase is decreased at a higher Nb concentration, and the alloy becomes less ductile. On the other hand, the addition of more Nb also increases the brittle eutectic phase. As a result, the alloy would undergo a larger thermal expansion, being more susceptible to cracking.

5. Summary and conclusions

The microstructure of Cr–Cr_2Nb intermetallic alloys as affected by thermal stresses has been analyzed. Cracking was observed in both as-cast and annealed specimens and was explained in light of the thermal stresses generated by spheroidal inclusions. Three cases for the inclusion systems were studied: the first is the Cr-rich particle embedded in the eutectic structure; the second, the Cr_2Nb inclusion in the Cr-rich matrix; and the third, the Cr-rich particle in the Cr_2Nb matrix. The numerical results show that the stress components at the interface for these cases are similar in characteristics, but different in magnitude and sign. The maximum tensile stresses are located at the interface when approaching from the Cr_2Nb phase in case two and case three and from the eutectic structure in case one. The maximum shear stress is always located at the semimajor axis approaching from the matrix. For all three cases, the calculated thermal stresses are sufficiently high to generate cracks in Cr–Cr_2Nb alloys.

Acknowledgements

S. Lee wishes to thank the National Science Council, Taiwan for financial support. The research was also sponsored by the Fossil Energy Advanced Research and Technology Development Materials Program and the Division of Materials Science, US Department of Energy, under contract DE-AC05-840R 21400 with Lockheed Martin Energy Research Corporation.

Appendix A

Consider a spheroidal inhomogeneity in an infinite matrix subjected to a temperature change T. Both the spheroid and the matrix are assumed to be elastically and thermally isotropic, and their shear moduli, Poisson's ratios and thermal expansion coefficients are denoted by μ^*, ν^*, α^* and μ, ν, α, respectively. The interface between the spheroid and matrix is assumed to be perfectly bonded. The spheroid in the Cartesian coordinate system (x_1, x_2, x_3) is defined by

$$\frac{x_1^2+x_2^2}{a^2}+\frac{x_3^2}{c^2}\le 1 \tag{1}$$

where a and c are the semimajor and semiminor axes, respectively.

Assuming $\nu=\nu^*$, the stress field is derived using the equivalent inclusion method proposed by Eshelby [10,11]. The internal stress components σ_{ij}^I inside the spheroid are constant, given by

$$\sigma_{11}^I=\sigma_{22}^I = \frac{2\mu(1+\nu)m(\alpha^*-\alpha)T}{(1-2\nu)(m-1)(RP-QS)}\{(S-m)(R-Q) + (R-\nu m)(P-S)\} \tag{2a}$$

$$\sigma_{33}^I=\frac{2\mu(1+\nu)m(\alpha^*-\alpha)T}{(1-2\nu)(m-1)(RP-QS)}\{(P-2\nu m)(R-Q) + (Q-m+m\nu)(P-S)\} \tag{2b}$$

where

$$P=2(m-1)[\nu(S_{1111}+S_{1122})+(1-\nu)S_{3311}]+2\nu \tag{3a}$$

$$Q=(m-1)[2\nu S_{1133}+(1-\nu)S_{3333}]+1-\nu \tag{3b}$$

$$R=(m-1)(S_{1133}+\nu S_{3333})+\nu \tag{3c}$$

$$S=(m-1)[S_{1111}+S_{1122}+2\nu S_{3311}]+1 \tag{3d}$$

$$S_{1111}=S_{2222}=\frac{3}{8(1-\nu)}\left[1-\frac{1+3M}{2(k^2-1)}\right] + \frac{1-2\nu}{4(1-\nu)}(1+M) \tag{3e}$$

$$S_{1122}=8\frac{1}{(1-\nu)}\left[1-\frac{1+3M}{2(k^2-1)}\right]-\frac{1-2\nu}{4(1-\nu)}(1+M) \tag{3f}$$

$$S_{1133}=S_{2233}=\frac{1}{4(1-\nu)}\frac{k^2(1+3M)}{k^2-1}-\frac{1-2\nu}{4(1-\nu)}(1+M) \tag{3g}$$

$$S_{3311}=S_{3322}=\frac{1+3M}{4(1-\nu)(k^2-1)}+\frac{(1-2\nu)M}{2(1-\nu)} \tag{3h}$$

$$S_{3333}=\frac{1}{2(1-\nu)}\left[1-\frac{k^2(1+M)}{k^2-1}\right]-\frac{(1-2\nu)M}{2(1-\nu)} \tag{3i}$$

$$M=\frac{1}{k^2-1}-\frac{k}{(k^2-1)^{3/2}}\cosh^{-1}(k) \quad \text{for } k\ge 1$$
$$=\frac{1}{k^2-1}+\frac{k}{(1-k^2)^{3/2}}\cos^{-1}(k) \quad \text{for } k<1 \tag{3j}$$

$$m=\frac{\mu^*}{\mu} \tag{3k}$$

Note that the aspect ratio, k, defined as c/a, is greater than, equal to, and smaller than unity for a prolate spheroid, sphere, and oblate spheroid, respectively.

The stress components outside the spheroid can be obtained as follows. Assume the oblate spheroidal coordinates (θ, ϕ, ψ) to be

$$x_1 = f \csc\theta \sin\phi \cos\psi \tag{4a}$$

$$x_2 = f \csc\theta \sin\phi \sin\psi \tag{4b}$$

$$x_3 = f \cot\theta \cos\phi \tag{4c}$$

in which $f = \sqrt{a^2 - c^2} > 0$ is the focal length. The range of θ, ϕ, and ψ are

$$0 < \theta \le \pi/2 \tag{5a}$$

$$0 \le \phi \le \pi \tag{5b}$$

$$0 \le \psi < 2\pi \tag{5c}$$

Using the equivalent inclusion concept of Eshelby [10–12], the thermally induced stress components are obtained, in terms of the transformation strain components, which are given by

$$e_{11}^T = e_{22}^T = \frac{R-Q}{RP-QS}(1+\nu)m(\alpha^* - \alpha)T \tag{6a}$$

$$e_{33}^T = \frac{P-S}{RP-QS}(1+\nu)m(\alpha^* - \alpha)T \tag{6b}$$

The thermal stress components outside the spheroid arising from the transformation strain e_{11}^T are obtained as:

$$\sigma_{11}^{(1)} = -\frac{\mu e_{11}^T}{4\pi(1-\nu)}\left\{3\Phi_{,11} + x_2\Phi_{,112} + \frac{1}{f^2}(a^2\Phi_{,11} + a^2x_3\Phi_{,113} - c^2\Phi_{,33} - c^2x_1\Phi_{,331})\right\} \tag{7a}$$

$$\sigma_{22}^{(1)} = \frac{\mu e_{11}^T}{4\pi(1-\nu)}\{\Phi_{,11} + x_2\Phi_{,112} + 2\nu\Phi_{,33}\} \tag{7b}$$

$$\sigma_{33}^{(1)} = \frac{\mu e_{11}^T}{4\pi(1-\nu)}\left\{2\nu\Phi_{,22} + \frac{1}{f^2}(a^2\Phi_{,11} + a^2x_3\Phi_{,113} - c^2\Phi_{,33} - c^2x_1\Phi_{,331})\right\} \tag{7c}$$

$$\sigma_{12}^{(1)} = \frac{\mu e_{11}^T}{8\pi(1-\nu)}\left\{x_2\Phi_{,111} - x_1\Phi_{,222} - 2\Phi_{,12} + \frac{1}{f^2}(c^2x_1\Phi_{,332} - a^2\Phi_{,12} - a^2x_3\Phi_{,123})\right\} \tag{7d}$$

$$\sigma_{13}^{(1)} = \frac{\mu e_{11}^T}{8\pi(1-\nu)}\left\{-x_1\Phi_{,223} - 4\Phi_{,13} + \frac{1}{f^2}(a^2x_3\Phi_{,221} - c^2x_1\Phi_{,223})\right\} \tag{7e}$$

$$\sigma_{23}^{(1)} = \frac{\mu e_{11}^T}{8\pi(1-\nu)}\left\{x_2\Phi_{,113} + \frac{1}{f^2}(c^2\Phi_{,23} + c^2x_1\Phi_{,123} - a^2x_3\Phi_{,112})\right\} \tag{7f}$$

where

$$\Phi = \frac{3V}{4f}\{\theta(3\cot^2\theta\cos^2\phi - \cot^2\theta + \cos^2\phi + 1) + \cot\theta(1 - 3\cos^2\phi)\} \tag{8a}$$

$$\Phi_{,11} = \frac{3V}{2f^3}\left\{\frac{\sin 2\theta(\csc^2\theta + \sin^2\phi\cos 2\psi)}{2g_o} - \theta\right\} \tag{8b}$$

$$\Phi_{,12} = \frac{3V}{4f^3g_o}\sin 2\theta \sin^2\phi \sin 2\psi \tag{8c}$$

$$\Phi_{,13} = \frac{3V}{2f^3g_o}\sin\theta \sin 2\phi \cos\psi \tag{8d}$$

$$\Phi_{,112} = \frac{3V\cos\theta\sin\phi\sin\theta}{f^4g_o}\left\{\sin^2\theta + \frac{(3 - 4\cos^2\theta)\sin^2\phi\cos^2\psi}{g_o} - \frac{4\cot^2\theta\sin^2\phi\cos^2\psi}{g_o^2}\right\} \tag{8e}$$

$$\Phi_{,113} = \frac{3V\sin^2\theta\cos\phi}{f^4g_o}\left\{1 + \frac{(1 - \cot^2\theta)\sin^2\phi\cos^2\psi}{g_o} - \frac{4\cos^2\theta\sin^2\phi\cos^2\psi}{g_o^2\sin^4\theta}\right\} \tag{8f}$$

$$\Phi_{,331} = \frac{3V\cos\theta\sin\phi\cos\psi}{f^4g_o^3}\{\csc^2\theta\sin^2\phi - \sin^4\phi - 4\csc^2\theta\cos^2\phi\} \tag{8g}$$

$$\Phi_{,123} = -\frac{3V\sin 2\phi\sin\phi\sin 2\psi}{4f^4g_o^2}\left\{\cos 2\theta + \frac{4\cot^2\theta}{g_o}\right\} \tag{8h}$$

$$g_o = \csc^2\theta - \sin^2\phi \tag{8i}$$

$$V = 4\pi a^2c/3 \tag{8j}$$

Here ϕ is the Newtonian potential and a subscript j after a comma represents the differentiation of the function with respect to the jth coordinate. Functions, $\Phi_{,22}$, $\Phi_{,23}$, $\Phi_{,332}$, $\Phi_{,223}$, and $\Phi_{,332}$ are obtained from $\Phi_{,11}$, $\Phi_{,13}$, $\Phi_{,112}$, $\Phi_{,113}$ and $\Phi_{,331}$ if $\cos\psi$ and $\sin\psi$ in Eq. (8) are exchanged with each other. Because the Newtonian potential Φ outside the spheroid satisfies the Laplace equation, $\Phi_{,33}$ and $\Phi_{,111}$ are found to be

$$\Phi_{,33} = -\Phi_{,11} - \Phi_{,22} \tag{8k}$$

$$\Phi_{,111} = -\Phi_{,221} - \Phi_{,331} \tag{8l}$$

and $\Phi_{,222}$ and $\Phi_{,333}$ are obtained by a cyclic permutation of (123) in Eq. (8l).

The stress field $\sigma_{ij}^{(2)}$ in the matrix arising from the transformation strain, e_{22}^T, can be found from Eq. (7) if subscripts, 1 and 2, are exchanged. The stress components in the matrix arising from the transformation strain, e_{33}^T, are

$$\sigma_{11}^{(3)} = \frac{\mu v e_{33}^{T}}{2\pi(1-v)}\Phi_{,22} + \frac{\mu e_{33}^{T}}{4\pi(1-v)f^2}\{a^2\Phi_{,11} + a^2x_3\Phi_{,113} - c^2\Phi_{,33} - c^2x_1\Phi_{,331}\} \tag{9a}$$

$$\sigma_{33}^{(3)} = \frac{\mu e_{33}^{T}}{4\pi(1-v)f^2}\{(4c^2-a^2)\Phi_{,33} + c^2(x_1\Phi_{,331} + x_2\Phi_{,332}) + a^2x_3\Phi_{,333}\} \tag{9b}$$

$$\sigma_{12}^{(3)} = -\frac{\mu v e_{33}^{T}}{2\pi(1-v)}\Phi_{,12} + \frac{\mu e_{33}^{T}}{4\pi(1-v)f^2}\{a^2\Phi_{,12} + a^2x_3\Phi_{,123} - c^2x_1\Phi_{,332}\} \tag{9c}$$

$$\sigma_{13}^{(3)} = \frac{\mu e_{33}^{T}}{8\pi(1-v)f^2}\{5c^2\Phi_{,13} + 2a^2x_3\Phi_{,331} + c^2(x_1\Phi_{,113} + x_2\Phi_{,223} - x_1\Phi_{,333})\} \tag{9d}$$

The components, $\sigma_{22}^{(3)}$ and $\sigma_{23}^{(3)}$, are found from $\sigma_{11}^{(3)}$ and $\sigma_{13}^{(3)}$ in Eqs. (9a) and (9d), if subscripts 1 and 2 are exchanged. The total stress components outside the spheroid are, then, given by

$$\sigma_{ij} = \sigma_{ij}^{(1)} + \sigma_{ij}^{(2)} + \sigma_{ij}^{(3)} \tag{10}$$

The above equations are also valid for the prolate spheroid coordinates, if f and θ are replaced by if and $i\theta$ where the range of θ is $(0, \infty)$ and $i = \sqrt{-1}$. Therefore, the solution based on the oblate spheroid coordinates can be easily transformed to that based on the prolate spheroid coordinates.

References

[1] H.J. Goldschmidt, J.A. Brand, J. Less-Common Met. 3 (1961) 44.
[2] A.I. Taub, R.L. Flescher, Science 243 (1989) 616.
[3] M. Takeyama, C.T. Liu, Mater. Sci. Eng. A132 (1991) 61.
[4] D.J. Thoma, J.H. Perepezko, Mater. Sci. Eng. A156 (1992) 97.
[5] J.A. Cook, P.K. Liaw, C.T. Liu, in: W.O. Soboyejo, T.S. Srivatsan, R.O. Ritchie (Eds.), Symposium on Fatigue and Fracture of Ordered Intermetallic Materials, TMS, Warrendale, PA, 1995, pp. 155.
[6] C.T. Liu, P.F. Tatorelli, J.A. Horton, C.A. Carmichael, Mater. Sci. Eng. A214 (1–2) (1996) 23.
[7] J.A. Cook, P.K. Liaw, C.T. Liu, S.B. Bhaduri, in: R.J. Arsenault, D. Cole, T. Gross, G. Kostorz, P. Liaw, S. Parameswaran, H. Sizek (Eds.), The Johannes Weertman Symposium, TMS, Warrendale, PA, 1996, pp. 47.
[8] J.H. Zhu, P.K. Liaw, C.T. Liu, Mater. Sci. Eng. A239–240 (1997) 260.
[9] R.H. Edwards, J. Appl. Mech. 73 (1951) 91.
[10] J.D. Eshelby, Solid State Phys. 3 (1956) 89.
[11] J.D. Eshelby, Proc. R. Soc. Lond. A241 (1957) 376.
[12] T. Mura, Micromechanics of Defects in Solids, 2nd, Kluwer Academic, Boston, MA, 1987, p. 178.
[13] Metal Handbook, Properties and Selection: Nonferrous Alloys and Special-Purpose Materials, 10th ed., vol. 2, ASM International, Metal Park, OH.
[14] F. Chu, Y. He, O.J. Thoma, T.E. Michell, Scr. Met. Mater. 33 (1995) 1295.
[15] K.S. Kumar, C.T. Liu, Acta Mater. 45 (1997) 1671.
[16] M.R. Jackson, R.G. Rowe, D.W. Skelly, Mater. Res. Soc. Symp. Proc. 364 (1995) 1339.
[17] C. Zener, Fracturing of Metals, American Society for Metals, Metals Park, OH, 1948.
[18] A.H. Cottrell, Trans. Metal. Soc. AIME 212 (1958) 192.
[19] A.N. Stroh, Adv. Phys. 6 (1957) 418.
[20] K. Seo, T. Mura, J. Appl. Mech. 46 (1979) 568.
[21] G.E. Dieter, Mechanical Metallurgy, 3rd, McGraw Hill, New York, 1988, p. 79.
[22] S. Lee, Key Eng. Mater. 145–149 (1998) 135.
[23] Y.Z. Tsai, S. Lee, J. Appl. Phys. 81 (1997) 2089.